TU Delft

Delft University of Technology

Study of foam generation and propagation in fully characterized physical-model fracture

AlQuaimi, B. I.; Rossen, W. R.

DOI
10.1016/j.petrol.2018.06.025

Publication date
2019

Document Version
Final published version

Published in
Journal of Petroleum Science and Engineering

Citation (APA)
AlQuaimi, B. I., & Rossen, W. R. (2019). Study of foam generation and propagation in fully characterized physical-model fracture. *Journal of Petroleum Science and Engineering*, *175*, 1169-1181. https://doi.org/10.1016/j.petrol.2018.06.025

Important note
To cite this publication, please use the final published version (if applicable).
Please check the document version above.

Copyright
Other than for strictly personal use, it is not permitted to download, forward or distribute the text or part of it, without the consent of the author(s) and/or copyright holder(s), unless the work is under an open content license such as Creative Commons.

Takedown policy
Please contact us and provide details if you believe this document breaches copyrights.
We will remove access to the work immediately and investigate your claim.

This work is downloaded from Delft University of Technology.
For technical reasons the number of authors shown on this cover page is limited to a maximum of 10.

Green Open Access added to TU Delft Institutional Repository

'You share, we take care!' - Taverne project

https://www.openaccess.nl/en/you-share-we-take-care

Otherwise as indicated in the copyright section: the publisher is the copyright holder of this work and the author uses the Dutch legislation to make this work public.

Journal of Petroleum Science and Engineering 175 (2019) 1169–1181

Contents lists available at ScienceDirect

Journal of Petroleum Science and Engineering

journal homepage: www.elsevier.com/locate/petrol

Study of foam generation and propagation in fully characterized physical-model fracture

B.I. AlQuaimi[a,b,*], W.R. Rossen[a]

[a] Department of Geoscience and Engineering, Delft University of Technology, The Netherlands
[b] Saudi Aramco, Dhahran, Saudi Arabia

ARTICLE INFO

Keywords:
In-situ foam generation
Foam in fracture
Mobility control in fracture
Pre-generated foam flow

ABSTRACT

Foam greatly reduces gas mobility for gas enhanced-oil-recovery (EOR) projects. It substantially increases both the effective viscosity of gas and gas trapping. Numerous studies have been conducted to understand foam rheology in rock matrix both theoretically and experimentally. The knowledge of foam flow in fractured porous media is incomplete, however. This study aims to contribute to the understating of foam generation and propagation in a fully characterized physical-model fracture. We investigate foam-generation mechanisms and the propagation of pre-generated foam. Gas mobility was greatly reduced as a result of in-situ foam generation. Foam-generation mechanisms similar to those seen in 3D porous media were observed on this model fracture. Foam was generated predominantly by capillary snap-off and lamella division. Lamella division was observed at high gas fractional flow at two different superficial velocities. Fracture wall roughness played an important role in foam generation. In the case of pre-generated foam, two very distinct bubble sizes were injected: fine-textured bubbles much smaller than the roughness scale and coarse-textured foam with bubbles much larger than the roughness scale. The first case did not show any significant change in bubble size as foam propagated through the model fracture, while in the second case, the fracture played a role in reducing bubble size. Inter-bubble diffusion did not regulate bubble size in our apparatus because residence time in the fracture is relatively short. We cannot confirm that foam reached local equilibrium in our experiments, but we believe that local equilibrium lies between the cases of in-situ- and pre-generated foams.

1. Introduction

Naturally fractured reservoirs (NFRs) have been receiving more attention over the last few decades due to the vast reserves of crude they contain. NFRs are found in many countries around the globe, in almost every lithology (Aguilera, 1980; Narr et al., 2006). Over the last four decades NFRs in the USA, for instance, have been under primary production, water injection and CO_2 flood (Manrique et al., 2007). Tertiary recovery or enhanced-oil-recovery (EOR) methods, including the injection of miscible carbon dioxide, steam, or nitrogen, have been implemented or considered for these reservoirs to recover the oil by-passed or not displaced during primary production (Babadagli, 2001; Manrique et al., 2007; Bourbiaux et al., 2016a, 2016b).

However, these fluids impose challenges due to their density and viscosity differences compared to in-situ fluids (Kim et al., 2005). These differences cause gravity override and viscous instability and worsen channelling, all of which are much more pronounced in NFRs because of the high conductivity of fractures. A statistical review of the overall ultimate recoveries of 100 NFRs indicates that the recovery of NFRs is somewhat lower than those of many conventional reservoirs (Allan and Sun, 2003). Considerable oil reserves are not recovered because of the nature of these reservoirs, which is a strong motivation for considering the use of foam to mitigate the low oil recovery expected in gas injection EOR.

The following is a brief summary of the studies of foam EOR in single fracture or in multiple fractures.

Kovscek et al. (1995) investigated nitrogen, water and aqueous foam flow through two transparent replicas of natural rough-walled rock fractures with hydraulic apertures of roughly 30 μm and 100 μm, respectively. Radial-flow tests were done on these fractures, with an outer radius of 12 cm. The total flow rate of nitrogen ranged from 1 to 100 standard cm^3/min, which is equivalent to 0.0014–0.147 m/s at the outer radius. The pressure drop was recorded across the whole sample. Foam reduced gas mobility in the model fracture by a factor of 100–540 over a range of foam qualities from 60 to 99%. In-situ foam generation was reported and described in terms of a capillary snap-off mechanism

* Corresponding author. Department of Geoscience and Engineering, Delft University of Technology, The Netherlands.
E-mail address: bander.quaimi@saudiaramco.com (B.I. AlQuaimi).

https://doi.org/10.1016/j.petrol.2018.06.025
Received 9 August 2017; Received in revised form 23 April 2018; Accepted 9 June 2018
Available online 15 June 2018
0920-4105/ © 2018 Published by Elsevier B.V.

similar to that in matrix porous media.

Yan et al. (2006) experimentally investigated foam sweep efficiency, using pre-generated foam, in model fractures that were either single or parallel double (side-by-side) smooth slits. The slit consisted of two parallel glass plates, where the gap in between represents the aperture and the gasket thickness between the plates sets the aperture of the fracture. The apertures were 100, 200 and 300 μm for the single slit and a combination of 100/200 or 50/150 μm for the double slit. The double-slit model fracture was created by adding another thin glass sheet in between to create a narrower part of the slit. The total superficial velocities ranged from 0.001 to 0.20 m/s and the foam qualities ranged from 0.0 to 90%. Yan et al. concluded that pre-generated foam can greatly improve the sweep efficiency in the double-slit fracture system.

Skoreyko et al. (2011) developed a new foam model from laboratory and field data for a fractured reservoir. High- and low-permeability fractures were created in 12-cm-long core samples of 2.0 md Indiana limestone. Each core was sawn into two halves, from inlet to outlet, and artificial vugs were drilled on both sides of the fracture surface. The high-permeability fracture was created by increasing the number of vugs, with some vugs overlapping. The fracture aperture was 1340 μm, set by placement of metal balls between rock faces. Surfactant solution and gas were co-injected into these fractured samples. The total superficial velocities ranged from 1.7×10^{-4}-5.1×10^{-4} m/s with foam qualities of 25, 50 and 75%. The authors developed a model to match laboratory core-flood data and the field-pilot tests. The study did not observe foam generation directly but reported an increase in pressure drop indicating foam generation.

Haugen et al. (2012) conducted laboratory experiments using foam to reduce fracture transmissivity and improve the matrix sweep in fractured, low-permeability, oil-wet limestone rock. The experiments were done on 8.0-cm-long core plugs sawn, from inlet to outlet, by a circular saw and on a 14-cm-long fracture network cut using a band saw on a rectangular block. The fracture was held open by a 1000-μm spacer. The sawn core plug was confined in a core holder. The sawn block was coated with epoxy resin on four sides of the block and two opposing sides were used to fit fluid inlet and outlet ports. The injected foam qualities used were 90 and 92%. The total superficial velocities were around 1.0×10^{-4} and 4.2×10^{-4} m/s for the core and the block, respectively. Both pre- and in-situ-generated foams were tested. The results of the laboratory experiments showed an increase in oil recovery for the pre-generated foam, while no foam generation was observed in the cores or blocks of smooth-walled fractures and hence no incremental oil was gained if foam was not pre-generated.

Buchgraber et al. (2012) experimentally investigated the behavior of pre-generated foam flow in micromodels at various foam qualities and fluid velocities. The experiments were conducted in channels etched on 2 × 5 cm silicon chips. The first experiment used parallel smooth channels with apertures of 40 and 30 μm. The second experiment was conducted by injecting foam into a medium comprising smooth, adjacent square regions with apertures of 20 and 40 μm arranged in a checkerboard pattern. The third experiment was done on a uniform-aperture channel with a rough face. The gas superficial velocity ranged from 7.23×10^{-6}-0.0057 m/s and the liquid superficial velocity ranged from 2.9×10^{-5}-0.0017 m/s. Buchgraber et al. concluded that foam reduced gas mobility in these idealized uniform-aperture fractures, where foam was pre-generated. Foam generation by snap-off was observed at the step changes between 20- and 40-μm apertures.

Haugen et al. (2014) experimentally studied supercritical CO_2, pre-generated CO_2-foam, and N_2-foam injections in fractured samples. The goal of the study was to investigate the effect of pre-generated foam on oil recovery by reducing the flow through the fracture and thereby diverting flow to the matrix. The study used 13 core plugs, which were cut along the core length using a diamond-coated circular saw. The permeability of the fractured cores ranged from 319 to 2020 md. The fractured core plugs, with different fracture permeabilities, were re-assembled and placed in a core holder with overburden pressure. Foam was injected into the fractured core plugs. A constant foam quality of 90% was used in most of the tests. The results showed that gas and surfactant contributed to oil recovery during CO_2-foam injection under oil-wet conditions, compared to pure CO_2. The study did not investigate in-situ foam generation.

Steinsbø et al. (2015) extended the study of Haugen et al. (2014). Miscible CO_2 and CO_2-foam laboratory tests were performed to study enhanced oil recovery in fractured core samples. In this study, the cores were fractured using a band saw, which creates relatively smooth fractures. The cores were assembled using spacers between the core halves to maintain the fractures open at a uniform fracture aperture of 1000 μm. The tests were conducted on two cores. In the first, a fracture ran from inlet to outlet. The second core was assembled from three sections with a break between each. The first 2-cm inlet section is unfractured and ends in a fracture across the core, perpendicular to flow. This section, in effect, acts as a foam generator for fractures downstream. The second, 4-cm-long section, had a vertically oriented fracture. The last 4 cm of the core had a horizontally oriented fracture. The three sections were assembled in a hassler core holder. Foam was pre-generated in all these tests using a sand-pack or the unfractured section of the core. The total superficial velocities used were 3.34×10^{-5}, 0.0003, and 0.0006 m/s. The tested foam qualities were 80 and 90%. Steinsbø et al. concluded that foam increased the oil production rate and final recovery in all the experiments due to the increase in viscosity in the fracture, leading to more CO_2 invasion into the matrix.

Gauteplass et al. (2015) experimentally studied foam generation in 5 × 5 cm micromodels with an etching depth of 25 μm. The micromodel had upstream and downstream distribution channels which were considered as fractures because of their permeability contrast with the etched part of the model. Foam was pre-generated using sandstone or a metallic sieve in all the experiments. The total superficial velocity used was approximately 0.0009 m/s and foam quality ranged from 75 to 95%. Foam texture changes by snap-off were observed at the permeability discontinuities between the distribution channel and the etched part of the model (i.e., going abruptly from a wide to a narrow aperture). They concluded that foam becomes finer as it flows across a permeability contrast.

Fernø et al. (2016) experimentally investigated the generation of foam within a heterogeneous rock slab 31.2 cm long. A ball-peen hammer was used to fracture a marble block which was then re-assembled in a frame. The fracture aperture of the network was estimated to be 100–150 μm. The pressure drop was measured across the whole sample. The tested foam qualities ranged from 60 to 95%. The total superficial velocities used were 0.0003, 0.001, 0.0017 and 0.0028 m/s. The study found foam generation by snap-off as gas flowed from fractures into vugs. Ferno et al. concluded that foam significantly improved the sweep of the fractures and delayed gas breakthrough compared with pure gas injection. A shear-thinning behavior was observed during coinjection of gas and surfactant solution over the tested range of foam qualities.

Most of these studies discuss the behavior and benefits of pre-generated foam in a fracture. Only two studies address foam generation, in a 12-cm-diameter disk-shaped fracture and 31.2-cm-long fracture with some vugs (Kovscek et al., 1995; Fernø et al., 2016). In these tests, the pressure drop was measured across the whole sample with little information about pressure gradient and foam texture as a function of position. In this study, we investigate foam generation and propagation in a well-characterized model fracture, 40-cm-long, with 4 pressure measurements. Mechanisms of foam generation as well as bubble size can be observed directly along the fracture. Moreover, we compare in-situ-generated foam with pre-generated foam over foam qualities ranging from 25 to 97%.

1.1. Fracture physical model

We investigated different design alternatives used in the literature to perform fracture flow experiments. Sawed or fractured rock cores do not allow one to directly observe foam texture and generation mechanisms inside the rock sample. Microfluidic devices have limited size and feature abrupt changes in otherwise smooth faces. A third option is to design a fracture apparatus made of glass plates. Model fractures made of glass plates have been used to study foam and two-phase flow in fractures (Pruess and Tsang, 1990; Fourar et al., 1992; Pieters and Graves, 1994; Chen et al., 2004a, 2004b; Yan et al., 2006; Qian et al., 2011; AlQuaimi and Rossen, 2017b). The transparent nature of the glass provides the ability to observe the flow and investigate foam generation mechanisms. More importantly, it allows one to systematically vary roughness scales (magnitude of aperture, aperture variation and length scale over which aperture varies) and investigate the effect of these on foam generation, stability and mobility. The goal is to develop means to relate foam to the different fracture geometries encountered in field applications. This is the first report of a series; here we report on foam generation for the first of our model fractures.

We constructed a 40 × 10 cm model fracture that consists of a roughened plate to represent the fracture roughness and a top plate that is smooth, to allow direct observation of the flow. The roughened plate is 4 mm thick and was strengthened by attaching a 15 mm-thick plate of glass using ultraviolet light and DELO®-Photobond® glue (DELO, Windach, Germany). The thickness of the top glass plate was 15 mm as well. The thickness of the glass plates was estimated based on solid-mechanics calculations to prevent any glass deflection during the flow. This was also checked using a Probe Indicator (2 μm resolution) during the experiment. The roughened plate included two inlet ports that allow separate co-injection of gas and liquid. These inlet ports were connected to 8.0 × 2.0 × 0.04 cm entry regions milled into the roughened plate. Four pressure ports were equally spaced over a length of 36 cm and including the fluid outlet. The gap between the top plate and the rough surface represents the fracture aperture. The two glass plates were glued together around the edges using Araldite® 2014, which is an epoxy adhesive that has a tensile strength of 26 MPa at 23 °C. The fracture was mounted in a frame that can slide 50 cm in X and Y directions to allow for microscopic observation of flow in the whole 40 × 10 cm fracture. In all experiments reported here, the fracture was held horizontal.

1.2. Fracture characterization

The model fracture used here has a regular pattern to its roughness, as shown in Fig. 1 (a). It provides an initial case study of foam behavior prior to testing more complicated surface geometries (AlQuaimi and Rossen, 2017a, 2017c). The roughened glass sample was profiled using NPFLEX™ White Light Interferometer Optical Profiling (Philips Innovation Services, Eindhoven, The Netherlands), to quantify the spatial and vertical variations in height. A separate sample of the same glass was coated by depositing a layer of silver 150 nm to enhance the reflection. Since this is a regular pattern of roughness the measurement was performed on a 1.0 × 1.0 cm region of the glass with a lateral resolution of 3.6 μm (Fig. 1 (a)).

A fracture can be considered as a two-dimensional network of pore bodies (maxima in aperture) connected by throats (saddle points in the topography of Fig. 1 (b) between pore bodies) (Tsang, 1984; Pyrak-Nolte et al., 1988; Rossen and Kumar, 1992; Hughes and Blunt, 2001). Locations of minimum aperture (highest locations in the topography of Fig. 1 (b) are occupied by water at all times in our experiments.

Several methods are available in the literature to extract a realistic pore network description for matrix rock samples (Rabbani et al., 2014). The method we use is based on a simple concept using flood-fill and image slicing (AlQuaimi and Rossen, 2017a). A MatLab® (The MathWorks Inc., Eindhoven, The Netherlands) code was developed to highlight all areas with height less than some threshold and then produce images at every 5 μm increment in height. An isolated, deep region represents a pore body. When two regions join upon increasing height, the connection between them is a pore throat. The sequence of images is loaded into ImageJ, an open-source Java image-processing program, to identify the pore throats and draw the pore-body boundaries. The characteristic pore-throat aperture (d_t) is taken at the percolation threshold for the region studied, the characteristic pore-body aperture (d_b) is the average pore-body aperture, and the characteristic pore length (L_p) is the average pore-body length of the 2D network in the flow direction (Fig. 1 (b)).

We vacuum the model fracture and inject demineralized water to displace all the air from the system. We next measure the hydraulic aperture of the model fracture by incrementally increasing the water injection rate and recording the pressure. The rate-pressure relationship was used to estimate the hydraulic aperture (Witherspoon et al., 1980; Hakami and Larsson, 1996; Chen et al., 2004a; Ferno et al., 2016).

$$Q = \frac{1}{12}\frac{|\nabla P| w d_H^3}{\mu} \tag{1}$$

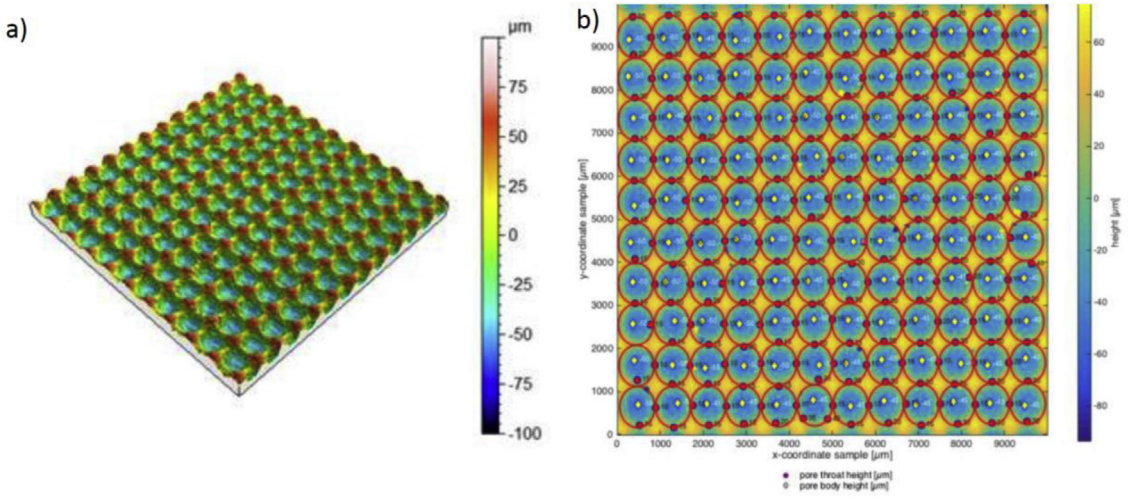

Fig. 1. (a) Bottom glass surface topography. Fig. 1. (b) 2D Network of pore bodies (blue) and pore throats (red). Region shown 1 × 1 cm. (For interpretation of the references to color in this figure legend, the reader is referred to the Web version of this article.)

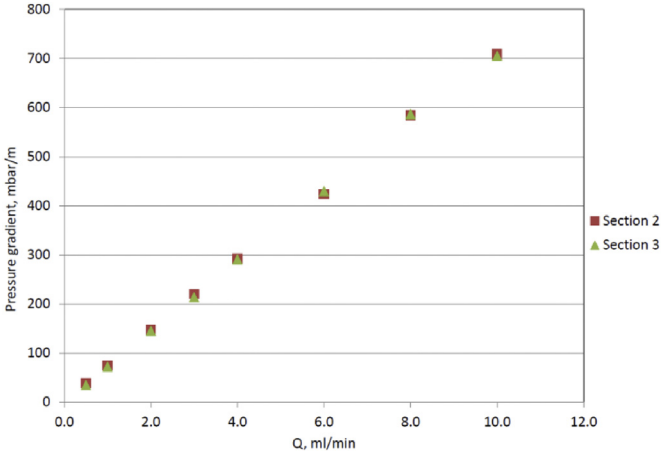

Fig. 2. Rate-pressure gradient relationship.

where Q is volumetric flow rate, $|\nabla P|$ is pressure gradient, w is the width of the fracture in the fracture plane, d_H is the hydraulic aperture, and μ is the viscosity. The flow experiments for our model fractures showed a linear relationship between Q and $|\nabla P|$, which indicates that the inertial forces were negligible and there was no change in aperture during flow (Fig. 2).

Table 1 summarizes the fracture-aperture data. The table also shows the characteristics of the rough surface. Additional details on the characterization of the fracture data are reported by AlQuaimi and Rossen (2017a).

1.3. Experimental setup

The model fracture discussed above is the centrepiece of the setup. Sodium C14-16 olefin sulfonate (Bio-Terge® AS-40 KSB, Stepan, Voreppe, France), an anionic surfactant with 39 wt.% active component and a critical micelle concentration of 301.0 mg/l, was used to generate foams. We prepared a surfactant solution of 1.0 wt.% in de-ionized water to be used in all the experiments. The surfactant solution is injected using a Standard Infusion PHD Ultra Syringe Pump (Model-703005, Harvard Apparatus, Holliston, MA, USA). Flow rates are stated to be accurate to within 0.25%, with reproducibility within 0.05% of full scale. This pump is equipped with micro-stepping techniques to further reduce flow pulsation. The pump has a range from 0.0001 µl/h to 216 ml/min.

Nitrogen is injected through a gas mass-flow meter/mass-flow controller (EL-Flow® F-230M-RAD-22-K, Bronkhorst High-Tech B.V., Ruurlo, Netherlands) which has a range of 0–10 Milliliter normal per minute (mln/min). The bottom glass plate includes four pressure ports with a distance of 9.0 cm between them, to provide pressure readings across the length of the apparatus. The pressure-difference sensors are signal-conditioned and temperature-compensated. These sensors (MPXV5050DP, Freescale Semiconductor, Inc., Austin, TX, USA) have a range from 0 to 50 kPa (0–7.25 psi) with a maximum error of 2.5% from 0 °C to 85 °C. The sensors are connected to a data-acquisition unit and a computer, where pressure is recorded every second.

For monitoring in-situ foam generation and foam texture a LEICA

Table 1
Fracture Aperture and roughness data (all in µm).

Pore-throat aperture, d_t	60
Pore-body aperture, d_b	130
Hydraulic aperture (experimentally determined), d_H	66
Pore Length, L_p	815
Arithmetic average absolute deviation from average aperture, S_a	29
Root-Mean-Square deviation from average aperture, S_q	34

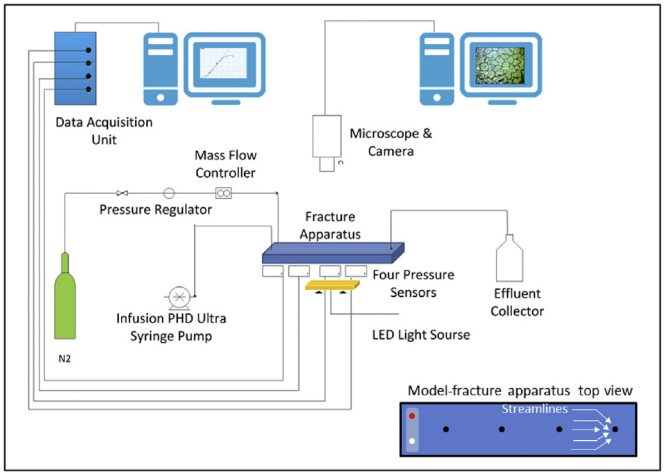

Fig. 3. Schematic of experimental setup.

MZ 8 Microscope (10445538 1.0X, Leica Microsystems B.V., Amsterdam, Netherlands) is used. The microscope is connected to DRS's lightning RDTTM camera, consisting of a small camera head, detachable cable and custom frame-grabber board. The lightning RDTTM is an ultrafast, high-resolution camera that captures 1280 1024-resolution images at 500 full frames per second (fps). Higher fps of 16,000 can be achieved at reduced resolution for recording extremely rapid events. MiDAS 2.0 camera-control software (Xcitex Inc., Woburn, MA, USA) is also used to process the images/videos in real time during recording. A compact backlight (model CVI STAR-BL-110/110-WH-24V; Stemmer® Imaging B.V., Zutphen, Netherlands) provides constant and even illumination. Uniform light is needed to produce noise-free images. Figs. 3 and 4 show the experimental setup.

1.3.1. In-situ foam generation

In the model fracture, foam was generated in situ by similar mechanisms to those observed in the 3D pre actworks of rock porous media. First, we vacuum-saturated the fracture with water (no surfactant), followed by co-injection of gas and surfactant solution. The gas remained in the entry region until the gas pressure exceeded the capillary entry pressure of the fracture. Leave-behind lamella generation was observed upon initial gas entry in the vicinity of the entry region, as gas displaces water, leaving lenses in the throats. Fig. 5 shows a sequence of images showing lens creation by leave-behind between gas entry paths. This foam was generated at 0.25 fractional flow of gas (f_g)

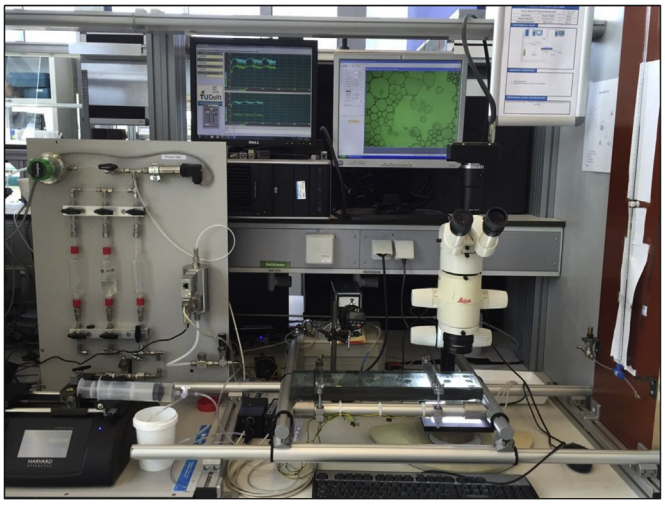

Fig. 4. Photo of the experimental setup.

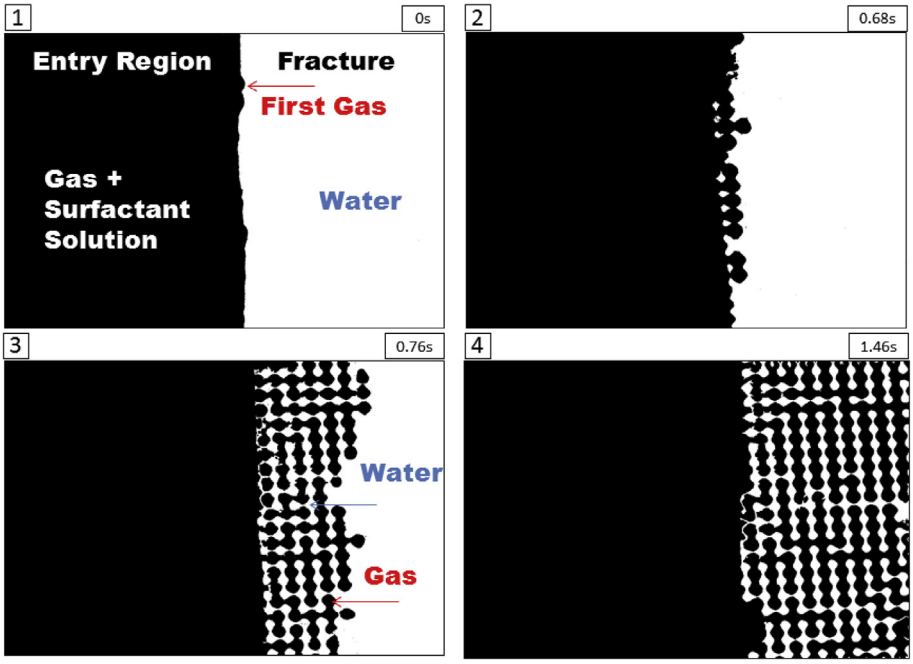

Fig. 5. A sequence of processed images (2.2 × 1.5 cm) that shows lens creation by leave behind. $f_g = 0.25$ and $u_t = 0.0021$ m/s. Black is gas and white is water. The images span a period of 1.46 s.

and total superficial velocity u_t of 0.0021 m/s.

Lamella division occurs when a film of a large bubble divides as it encounters a split in the flow path. Fig. 6 shows foam generation by lamella division at f_g of 0.88 and u_t of 0.0021 m/s. Lamella division was observed frequently at high f_g, especially when a foam bubble is larger than one pore body, which is 0.5 mm^2. In our experiment with this model fracture, we did not observe lamella division at low foam quality. We also tested a higher superficial velocity $u_t = 0.0049$ m/s and we observed lamella division at high f_g only.

At lower f_g (0.37), $u_t = 0.0021$ m/s, at a distance of 20 cm from the injection point, as the foam front advances, foam was generated by repeated capillary snap-off events, until the given pore fills with bubbles. Fine-textured foam was created at the front, with bubbles often smaller than the pore bodies and coarser foam behind (Fig. 7). Snap-off of bubbles much smaller than pores reflects in part the slit-shaped geometry of the pore throats (Rossen, 1996, 2003). For this model fracture the aperture at a pore throat d_t is much less than the width of the throat w. The capillary entry pressure is given by

$$P_c^e = \sigma\left(\frac{1}{\frac{w}{2}} + \frac{1}{\frac{d_t}{2}}\right) \cong \frac{2\sigma}{d_t} \tag{2}$$

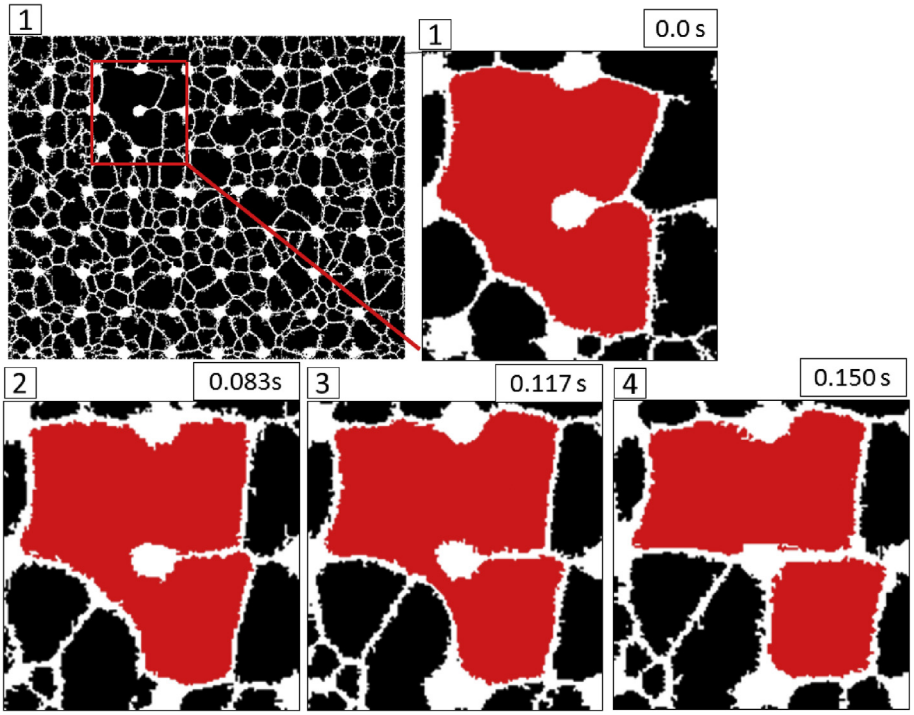

Fig. 6. A sequence of processed images (0.18 × 0.2 cm) of foam generation by lamella division $f_g = 0.88$ and $u_t = 0.0021$ m/s. Black is gas and white is water. The images span over a period of 0.15 s. The divided bubble is highlighted in red. (For interpretation of the references to color in this figure legend, the reader is referred to the Web version of this article.)

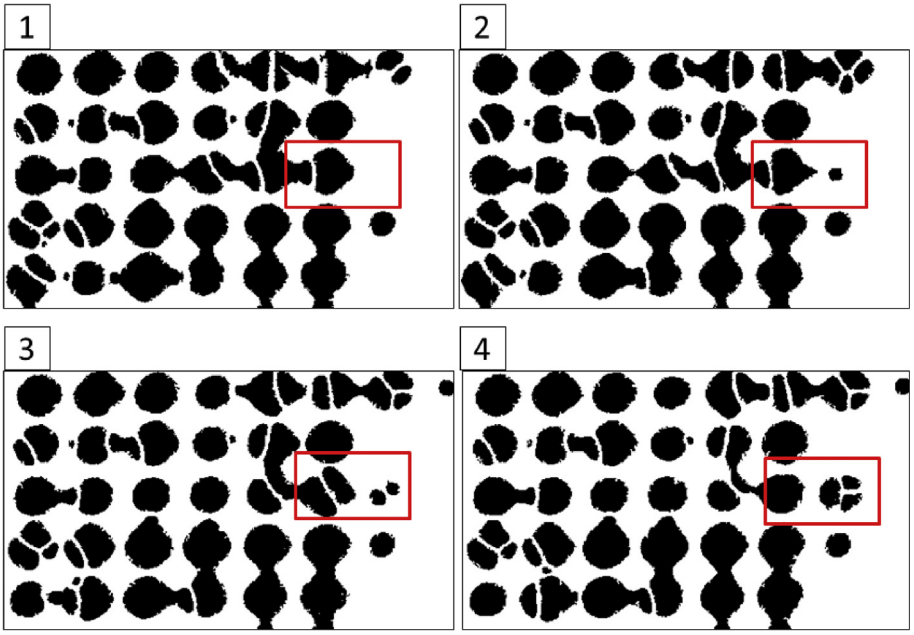

Fig. 7. A sequence of processed images (0.43 × 0.75 cm) that shows foam generation by capillary snap-off and foam propagation. $f_g = 0.37$, $u_t = 0.0021$ m/s. Black is gas and white is water. The red rectangle highlights the event. (For interpretation of the references to color in this figure legend, the reader is referred to the Web version of this article.)

where σ is the gas-liquid surface tension (Lenormand et al., 1983). The capillary pressure for snap-off P_c^{sn} is $(2\sigma/d_t)$. Pore-throat aperture d_t is approximately 60 μm (Table 1), and throats are approximately 400 μm wide in the other direction (cf. pore length in Table 1 and pore geometry in Fig. 1 (b). For this surfactant $\sigma = 0.031$ N/m and $d_t = 60$ μm; therefore $P_c^e \cong 11.9$ mbar and P_c^{sn} is 10.3 mbar. In this geometry, where a pore throat approximates a slit, the ratio of capillary pressure for snap off to capillary entry pressure (P_c^{sn}/P_c^e) approaches 1: a slight fluctuation in P_c can cause snap-off in such a throat.

In rock matrix bubbles are thought to be as large as pores (Alvarez et al., 2001), in part because diffusion rapidly eliminate smaller bubbles. Appendix A presents an analysis of inter-bubble diffusion, which is slower in a slit-like geometry and does not have time to operate in the bubble residence time (approximately 2.66 min) in our apparatus. Fig. 8 shows that bubbles typically advance on a scale of few seconds. A similar observation was reported for foam flow in fractures (Haugen et al., 2014; Fernø et al., 2016). Appendix A shows an experiment to estimate the time taken for a small bubble to disappear by diffusion. The experiment confirms that diffusion is very slow on the time scale of our experiment.

Liquid lenses are created by snap-off and leave-behind during initial gas invasion, but many of these break without surfactant to stabilize them. With surfactant, these lenses survive as they drain to lamellae, and the gas phase remains discontinuous. The liquid lamellae and lenses block the paths of continuous flow and hence this increases flow resistance. Fig. 9 shows trapped gas and the flow path of water in the case of no surfactant present. The mobility of both water and gas is much greater than if surfactant stabilizes the lamellae formed in two-phase flow.

1.3.2. Foam propagation

In general, underground rock fractures are large features which could span the reservoir height and extend hundreds of meters horizontally (Bertotti et al., 2005; Ozkaya, 2007). Thus, foam re-generation and propagation far into the reservoir is critical for the success of the foam-injection process. We monitored bubble texture of the foam across the fracture at steady-state flow conditions. This test was conducted at $f_g = 0.37$, $u_t = 0.0021$ m/s and 1.0 wt.% surfactant solution. Fig. 10

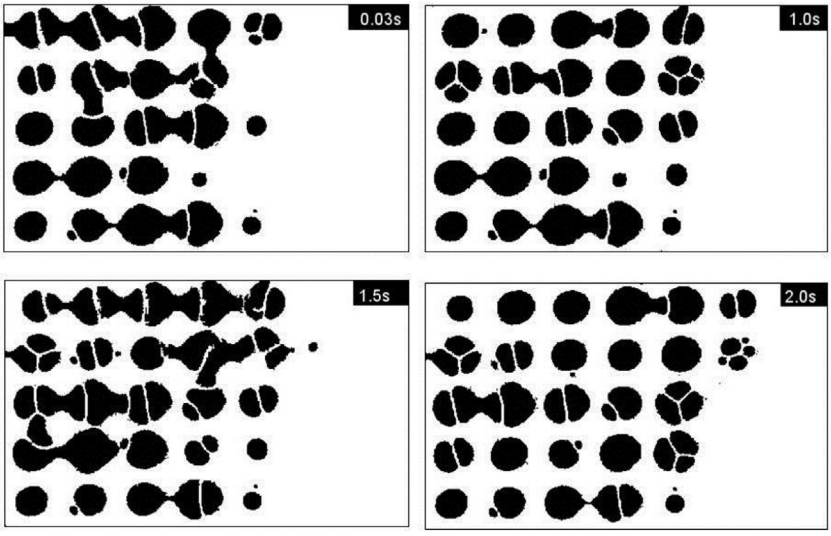

Fig. 8. A sequence of processed images (0.45 × 0.75 cm) that shows movement of bubbles.

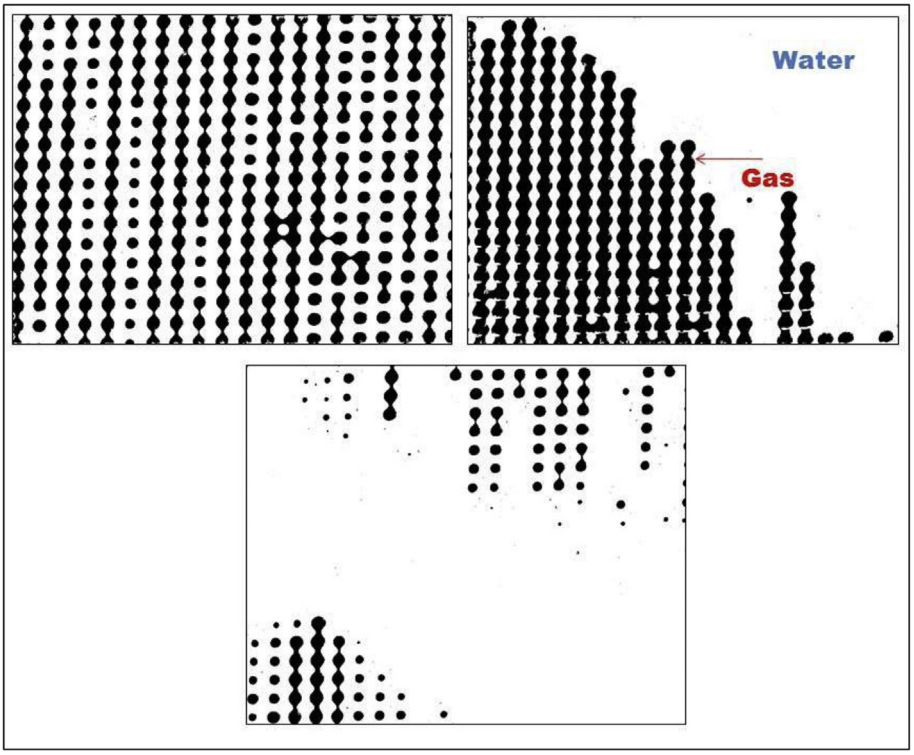

Fig. 9. Images (2.0 × 1.5 cm) show gas and water flow (No surfactant); (same-color) f_g (0.37), u_t = 0.0021 m/s. The bottom image shows that water advances in separate paths from gas. Flow is from left to right. Images were captured at three locations. (For interpretation of the references to color in this figure legend, the reader is referred to the Web version of this article.)

illustrates foam bubble texture at steady state from three locations, at 20, 120 and 270 mm from the injection port. The images demonstrate that finer foam continues to be generated as it propagates through the fracture. Table 2 shows that the number of bubbles per unit area of fracture almost doubles toward the end of the model fracture. As noted, at this low value of f_g (0.37), the dominant mechanism of lamella creation is snap-off. The pressure gradient increases as more bubbles are created. Thus the "entrance effect" seen in 3D porous media (Ettinger and Radke, 1992) extends 10's cm in our model fracture. Fig. 11 shows the evolution of the pressure drop across the entire fracture. The pressure gradient in the first section is affected by the entry region and the last one by the converging flow towards the outlet (Fig. 3), so they were not used in the analysis. Thus, we select the third section to base our comparison of the pressure-gradient behavior. We cannot directly confirm from these data that foam is at local equilibrium in the third section (see below), but it is our best basis of comparison. Fig. 12 compares steady-state pressure gradient for pure gas injection, water injection, coinjection of gas and water (no surfactant) and foam (gas and surfactant solution). A much greater pressure gradient was achieved when foam was injected compared to the other cases.

Table 2
Image-analysis statistics from Fig. 10. The number of bubbles per unit area of fracture almost doubles towards the end of the model fracture.

Section	1	2	3
Distance from inlet, mm	20	120	270
Average bubble size, mm^2	0.250	0.138	0.081
Bubble size, std. dev., mm^2	0.205	0.125	0.056
Number of bubbles per unit area	165	217	303

Fig. 10 shows that bubble size decreases as foam flows along the fracture. It also shows that the fraction of the fracture area covered by water increases downstream. Water saturation S_w is monotonic with the area fraction covered by water, though we do not have the exact conversion from area fraction to saturation. Since pressure gradient is larger downstream, this implies that water relative permeability k_{rw} decreases as water saturation increases downstream. In 3D porous media, it is often reported that the k_{rw} (S_w) function is unaffected by foam (Bernard and Holm, 1964; Holm, 1968; Huh and Handy, 1989), and this assumption underlies most foam simulation models. It is evidently not the case here, since k_{rw} decreases as S_w increases.

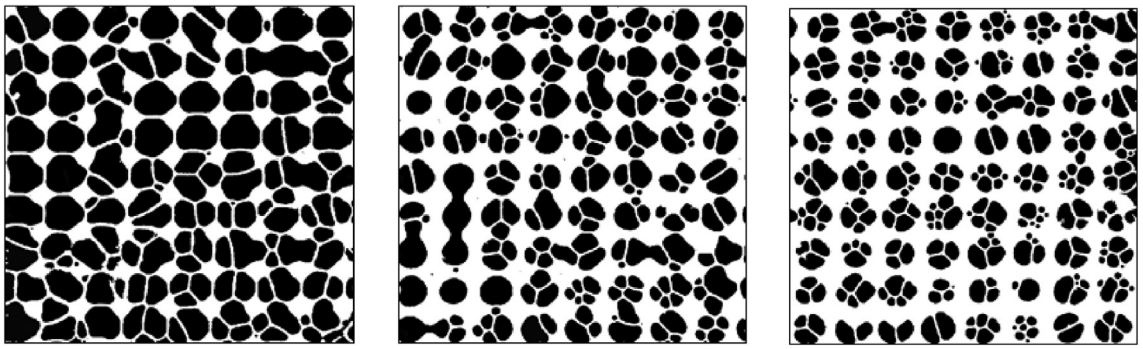

Fig. 10. 0.8 × 0.77 cm images of foam texture vs distance from the injection point after the steady-state pressure gradient is achieved (Fig. 11). f_g = 0.37, u_t = 0.0021 m/s. Left: section 1; middle: section 2; right: section 3.

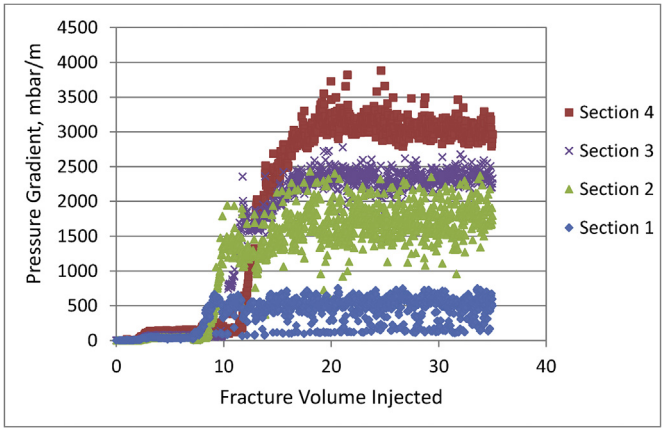

Fig. 11. Pressure gradient along the model fracture; f_g of 0.37, u_t of 0.0021 m/s.

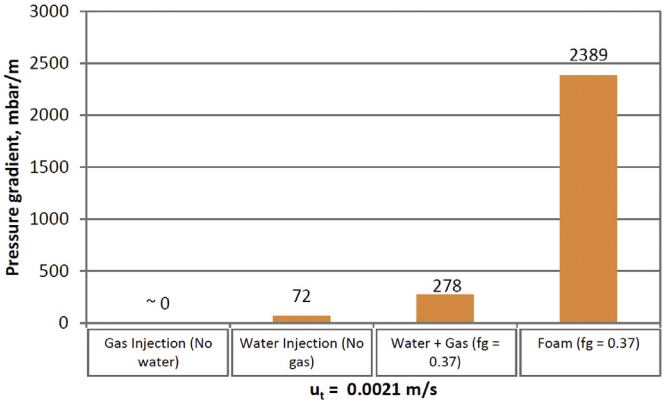

Fig. 12. Pressure gradient for foam injection compared to gas, water and co-injection of gas and water. Pressure gradient with gas alone was too small to measure.

It could be argued that the capillary entry pressure explains the accumulation of water in sections 2 and 3 in Fig. 10. However, the capillary entry pressure, as noted above, is approximately 11.9 mbar. The pressure difference in Section 4 alone (cf. Fig. 11) is approximately 270 mbar, greatly exceeding the capillary entry pressure. Therefore, the impact of the capillary end effect on sections 2 and 3 is expected to be modest.

We performed foam-quality scans, where u_t is fixed and f_g is varied (Fig. 13). The left-hand vertical axis shows foam apparent viscosity (μ_{app}) at different foam quality, with highest apparent viscosity at $f_g = 0.62 = f_g^*$. μ_{app} is calculated using Eq. (3)

$$\mu_{app} = \frac{1}{12}\frac{|\nabla P| w d_H^3}{Q} \tag{3}$$

where $|\nabla P|$ is pressure gradient, w is the width perpendicular to flow, d_H is the hydraulic aperture, and Q is volumetric flow rate. The data points have numbers which indicate the sequence at which they were acquired. This sequence was chosen to avoid possible hysteresis that might occur in case of sequential increase or decrease in f_g. The value near zero for $f_g = 0$ represents the viscosity of water injection with no gas present. Additionally, point 7 at f_g of 0.25 was repeated after displacing all the foam and starting the experiment with the initial condition of only water in the fracture. This gives extra confidence in the measurement and the procedure followed to acquire the data. The error bars in μ_{app} data reflect oscillations in pressure gradient (cf. Fig. 11).

At high quality, we observed a cycle in which fine-textured foam is generated and propagates, followed by a slug of gas that is refined as it propagates. This causes the pressure response to fluctuate and hence reduces time-average foam apparent viscosity. In nonfractured porous

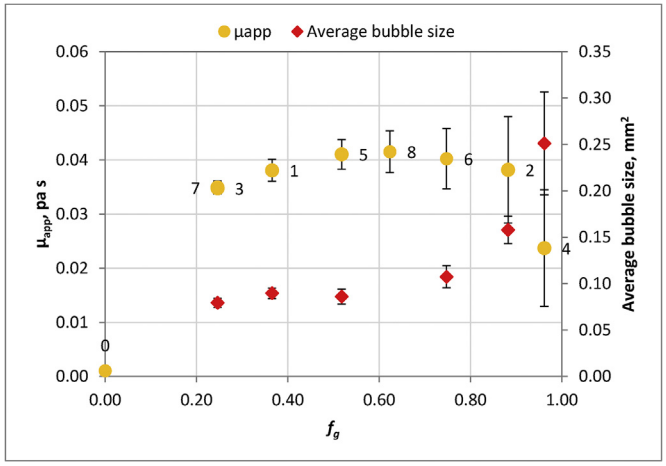

Fig. 13. Foam apparent viscosity μ_{app} and average bubble size over a range of foam qualities; ut = 0.0021 m/s. Error bars in μ_{app} reflect fluctuations in pressure gradient. Error bars in bubble size indicate standard deviation in the bubble size.

media the decrease of foam apparent viscosity at high quality is believed to reflect destruction of foam at a limiting capillary pressure (Khatib et al., 1988; Ransohoff and Radke, 1988; Alvarez et al., 1999). In our results, in contrast, it reflects less efficient foam generation. The right-hand vertical axis (red symbols) shows the average bubble size determined from images taken at the stabilized pressure gradient (cf. Fig. 13) in Section 3. The average bubble size correlates inversely with the pressure gradient, as expected; the error bar is the standard deviation of the average bubble size. The standard deviation of the bubble size increases with the increase in f_g due to reduced and fluctuating foam generation. Fig. 14 shows that foam-bubble shape becomes polyhedral at high foam quality.

1.3.3. Injection of pre-generated foam

We investigated the behavior of pre-generated-foam flow in our model fracture. Foam was generated upstream of the fracture apparatus using foam-generator filters. We selected two very distinct sizes of filters, with openings of 7 and 400 μm, to generate two different foams. In the flow of bulk foam through the tubing and in the entrance port, bubbles are expected to grow by inter-bubble diffusion (Nonnekes et al., 2015). In our experiments the bubbles grew considerably before they reached the model fracture. Bubbles initially 7 μm in size were still smaller than pores as they entered the fracture. Bubbles of initially 400 μm grew to sizes much greater than the pore size in the fracture. The experimental setup was the same except for the filter added upstream of the model fracture. The surfactant solution and nitrogen were injected through two different lines to the filter where foam was generated.

The same experimental conditions were used in each case. The fracture was fully saturated with water (no surfactant). Surfactant solution (1.0 wt.%) was injected with nitrogen through the filter, at $f_g = 0.37$ and a superficial velocity $u_t = 0.0021$ m/s. With the 7-μm filter, foam bubbles were already considerably smaller than the pore throats (flow restrictions), so foam was not refined by snap-off. The foam front advanced steadily as bubbles filled each pore body (Fig. 15). Small bubbles advanced ahead of larger bubbles (Fig. 15).

When pressure gradient reached steady-state, foam texture was investigated. Images were captured in the different sections between the injection port and the outlet. Section 1 had the greatest number of large bubbles, which advanced at a much lower velocity. Section 4 was affected by the converging flow into the production port. The average foam bubble size in sections 2 and 3 is nearly the same (Fig. 16 and Table 3).

The 7-μm filter generates very fine foam; thus, we selected the

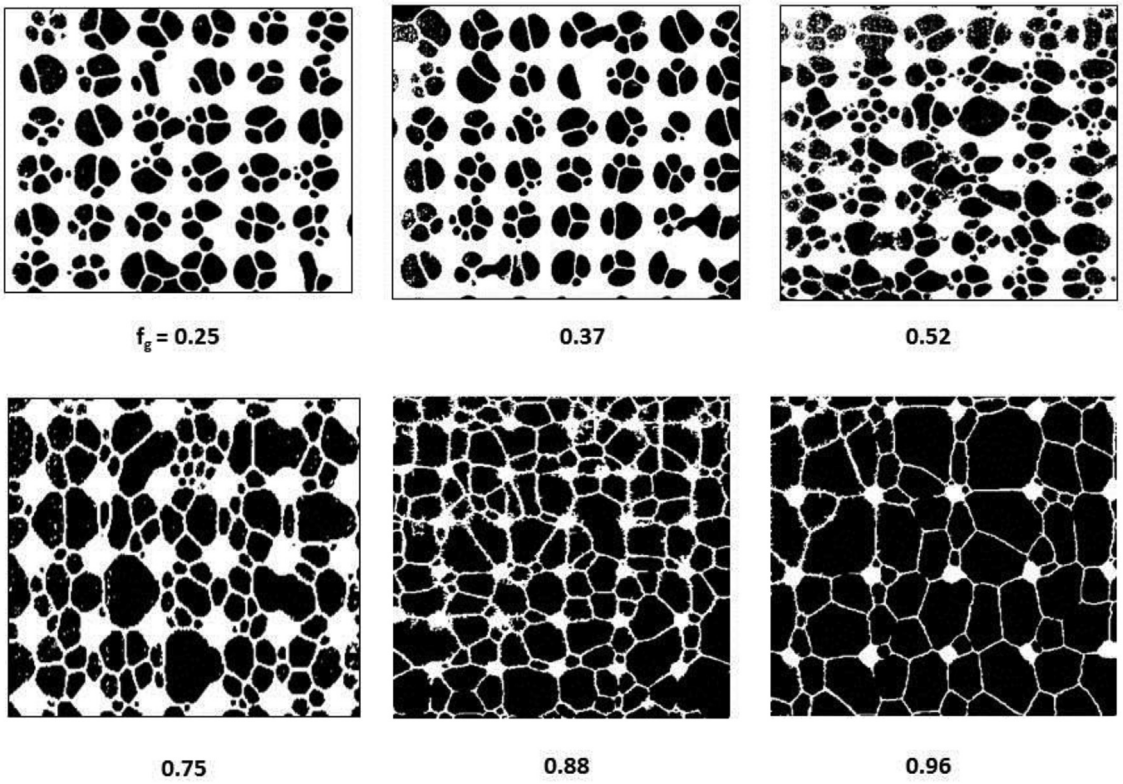

Fig. 14. Foam texture vs f_g (White is water and black is gas). Images were captured with the stabilized pressure gradient, 270 mm from injection port). Image size is not identical in each case, but it is of the order 0.4 × 0.48 cm.

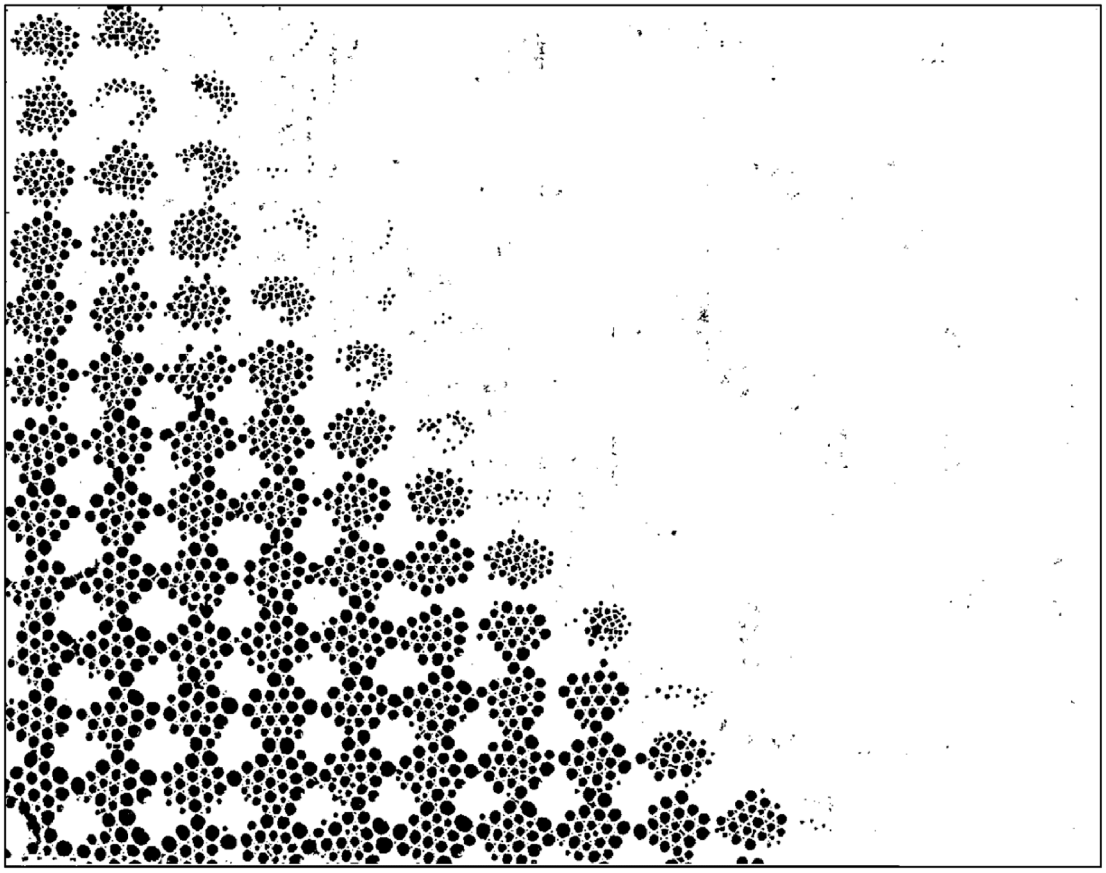

Fig. 15. Foam texture near the advancing front of foam pre-generated using a 7-μm filter. 1.4 × 1.5 cm image of foam front (f_g = 0.37). Flow is from left to right. The front has advanced further at the bottom of the image, but all along the front small bubbles advance ahead of larger ones.

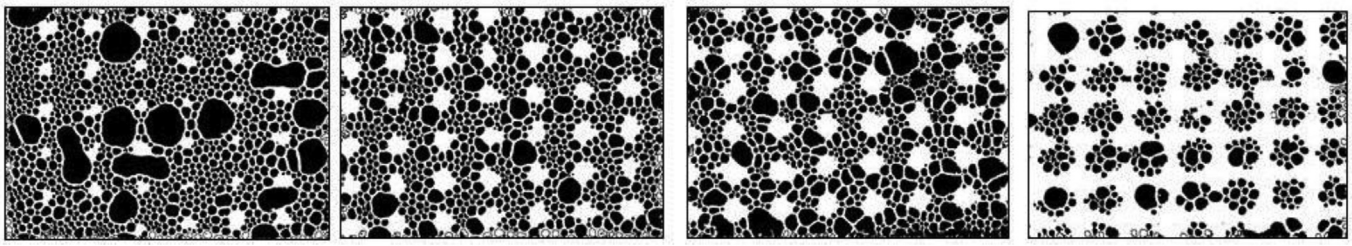

Fig. 16. Foam texture vs distance; $f_g = 0.37$, $u_t = 0.0021$ m/s (black is gas and white is water. Images were captured during stabilized pressure gradient.) Image size 0.7 × 0.5 cm. Foam pre-generated using a 7-μm filter.

Table 3
Image-analysis statistics of the foam pre-generated using 7-μm filter.

Section	1	2	3	4
Distance from inlet, mm	20	120	270	360
Average bubble size, mm^2	0.028	0.024	0.028	0.024
Bubble size, std. dev., mm^2	0.060	0.026	0.034	0.028
Number of bubbles per unit area	701	677	564	448

400 μm filter for the second pre-generated-foam experiment. We retained the same experimental conditions as in the previous test. The model fracture was thoroughly cleaned and saturated with water (no surfactant). Foam was injected at $f_g = 0.37$, $u_t = 0.0021$ m/s. The pre-generated foam contains bubbles much larger than the pores by the time foam reaches the fracture. The large pre-generated bubbles are sequezed into disk-like shapes in the reservoir upstream of the fracture (Fig. 17). The large bubbles divide by capillary snap-off as they enter the fracture, and they occupy one or more pores. Analysis of images along the fracture (Fig. 18) shows that average foam bubble size deceases as one moves downstream. Foam becomes finer due to snap-off as foam propagates forward. Consequently, the number of bubbles increases 2.3-fold up to Section 3, excluding the possible effects of converging flow in Section 4 (Table 4).

Fig. 19 compares foam apparent viscosity from all three tests. The apparent viscosity of the in-situ-generated foam is comparable to the pre-generated foam. The model fracture continues to make the texture finer as foam propagates downstream. The model fracture is expected to make finer-textured foam until generation and destruction mechanisms are at equilibrium. We have not reached the final foam equilibrium state in the case of in-situ-generated foam. However, since the properties of the fine-textured pre-generated foam and in-situ-generated foam are converging toward each other, we contend that steady-state texture is likely within this range.

1.3.4. Summary and conclusions

This is the first report of a larger study of foam in fractures for EOR using a variety of model fractures with different geometries. The following conclusions can be drawn:

1. Foam was generated in this 40 × 10 cm model fracture mainly by capillary snap-off: fracture-wall roughness played a major role in foam generation. Snap-off is less dominant at high injected gas fraction (f_g).
2. Lamella division was observed at high f_g at two different total superficial velocities.
3. Bubbles smaller than the pores were generated and propagated through the fracture. This depends in part on the geometry of the pore throats. Slit-shaped throats can give bubbles much smaller than pore bodies. The size of the bubbles is not always similar to the size of the pores because bubbles reside in the pore for a time that is

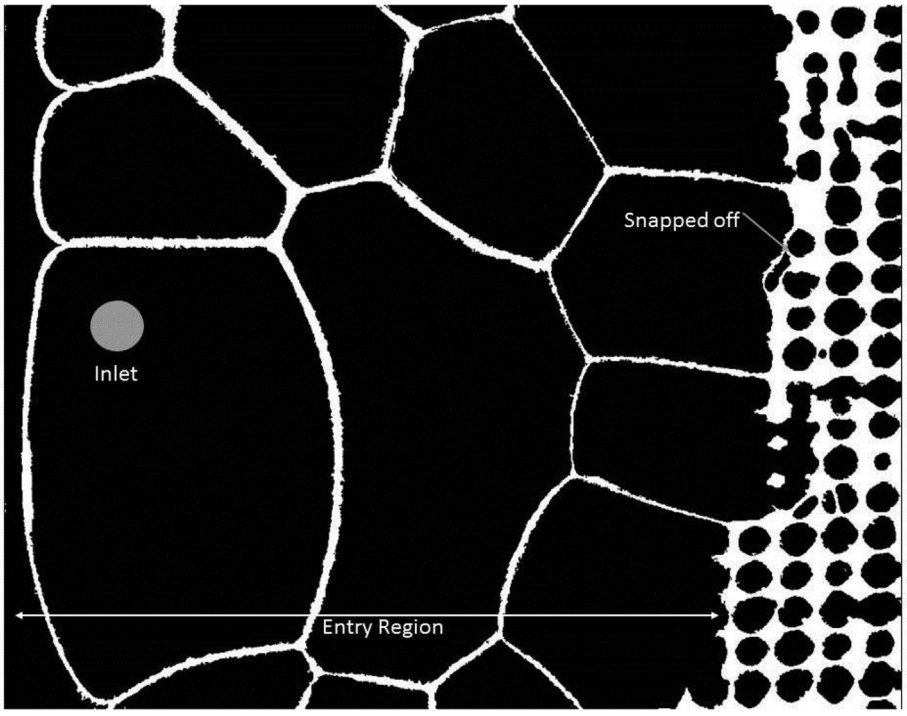

Fig. 17. Image of entry reservoir and entrance of fracture for foam pre-generated using 400-μm filter. Image size 2.0 × 1.6 cm. ($f_g = 0.37$, $u_t = 0.0021$ m/s.)

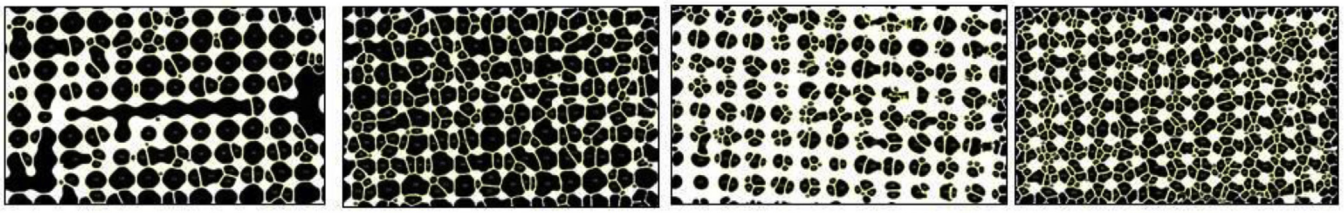

Fig. 18. Foam texture vs distance; $f_g = 0.37$, $u_t = 0.0021$ m/s. White is water while black is gas. Images were captured during the stabilized pressure gradient. Image size 1.21 × 0.75 cm. Foam pre-generated using a 400-μm filter.

Table 4
Image-analysis statistics of the foam pre-generated using 400-μm filter.

Section	1	2	3	4
Distance from inlet, mm	20	120	270	360
Average bubble size, mm^2	0.343	0.250	0.107	0.100
Bubble size, std. dev., mm^2	0.439	0.175	0.072	0.068
Number of bubbles per unit area	132	227	305	486

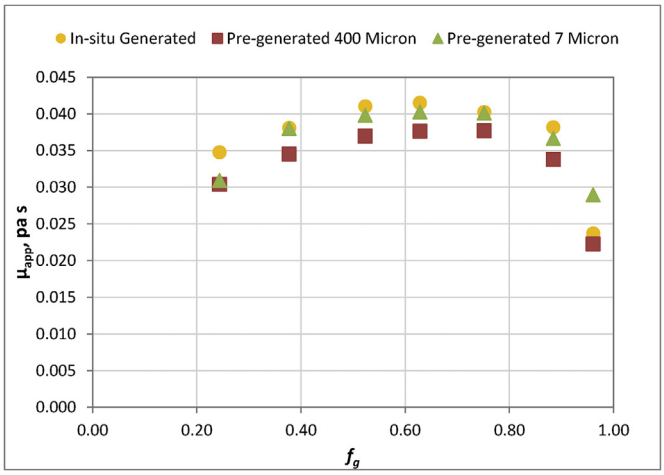

Fig. 19. Foam apparent viscosity as a function of foam quality at $u_t =$ = 0.0021 m/s of in-situ, and pre-generated foams. The standard deviations of foam apparent viscosity are approximately 0.0009 and 0.01 Pa s at low quality and high quality, respectively.

much shorter than the time required for diffusion to eliminate smaller bubbles. The pressure gradient correlates inversely with the average size of the bubbles.

4. For in-situ-generated foam, the pressure gradient correlates inversely with the average size of the bubbles.
5. Oscillations in pressure gradient were observed at high f_g due to reduced and fluctuating foam generation. Similar oscillations are observed in 3D matrix porous-media, but in that case are due to bubble destruction at the limiting capillary pressure.
6. This oscillation is also evident in the bubble sizes; bubble-size standard division increases as f_g increases.
7. Foam may not have reached final local equilibrium within the length of our apparatus but we contend that it is bounded between the results for fine-textured pre-generated foam and in-situ-generated foam.

Acknowledgment

The authors acknowledge Saudi Aramco for providing the scholarship for Mr. AlQuaimi, and also the generous support provided by the sponsors of the Joint Industry Project on Foam for Enhanced Oil Recovery at Delft University of Technology.

Appendix A. Time for coarsening of foam in a fracture

Consider for simplicity a single disk-shaped bubble of radius R between parallel plates, surrounded by a lamella and plateau borders along the plates. The curvature in the plane of the disk is (1/R). For simplicity we neglect variations in the gap h between the plates. The rate of molar gas transfer through the lamella is given by

$$W = k_s \Delta c A \tag{A-1}$$

where W is the molar transfer rate, K_s is the mass transfer coefficient, Δc is the molar concentration difference in the gas on opposite sides of the lamella, and A is the lamella surface area ($\sim 2\pi Rh$) (Cussler, 2009). Δc can be related to pressure through the ideal gas law:

$$\Delta c = \frac{\Delta p}{R_{ID} T} \tag{A-2}$$

where Δp is the pressure difference across the lamella, R_{ID} is the ideal-gas constant, and T is the absolute temperature. Δp can be calculated based on the capillary pressure difference across a cylindrical bubble between parallel plates:

$$\Delta p = \frac{\gamma}{R} \tag{A-3}$$

where γ is the surface tension and R is the radius. A mass balance on the bubble yields the following expression:

$$\frac{dV}{dt} = 2\pi h R \frac{dR}{dt} = -\frac{W}{c} \tag{A-4}$$

$$\frac{dR^2}{dt} = \frac{-2k_s\gamma}{cR_{ID}T} \tag{A-5}$$

The solution of this equation for a bubble initially with radius R_o is

$$R_0^2 - R^2 = \frac{-2k_s\gamma}{P}t \tag{A-6}$$

where P is the pressure which we assume for simplicity to be constant, R is the bubble radius at time t until the bubble disappears. K_s is 3.8×10^{-4} m/s for nitrogen gas with the surfactant solution we used (Farajzadeh et al., 2011), γ *is* 0.03 N/m and we take $P \approx 1.5 \times 10^{-5}$ Pa (cf. Fig. 11). An isolated bubble initially of 200 μm radius disappears by diffusion of gas into its surroundings in 4–5 min. This is only a rough estimate of diffusion time in our fracture but it is greater than the bubble residence time (typically 2–3 min) in our fracture. This estimate applies to diffusion through a lamella in a dry foam. Diffusion through a comparatively thick liquid lens would be much slower, which explains the survival of the tiny bubbles in Fig. 15, for instance.

We also observed the time for a small bubble to disappear by gas diffusion through lamellae in our model fracture. One cannot observe diffusion in rapidly flowing bubbles; therefore, we stopped the injection and waited for the bubble movement to stop. We started to record time and capture images. Fig. A-1 shows a sequence of images illustrating bubble disappearance by gas diffusion. The bubbles eventually occupy entire pores by diffusion, as expected. We color some bubbles in red to highlight their disappearance by diffusion. The length of the big bubble, which disappears completely in 10 min, is 270 μm. Its small neighbor disappears in 2–3 min. This bubble resides in a pore throat between much larger bubbles in the pore bodies. Therefore, curvature in the direction perpendicular to the glass plates (from variation in aperture) may have increased the pressure difference and diffusion rate. Diffusive coarsening between similar-size bubbles in pore bodies would be expected to be slower.

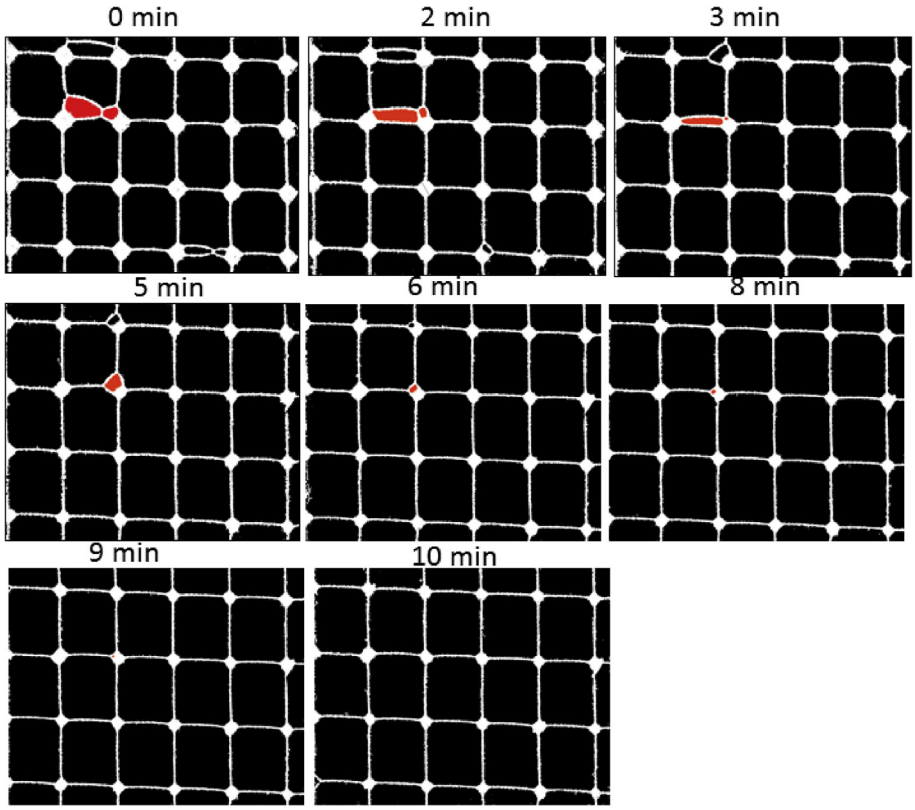

Fig. A-1. A sequence of images that shows the time required for a bubble to disappear by gas diffusion. Image size is 0.44 × 0.35 cm; black is gas and white is water. A bubble of interest, highlighted in red, disappears in about 10 min.

References

Aguilera, R., 1980. Naturally Fractured Reservoirs. Petroleum Publishing Company, Tulsa, Okla.

Allan, J., Sun, S.Q., 2003. Controls on recovery factor in fractured reservoirs: lessons learned from 100 fractured fields. In: Paper Presented at the SPE Annual Technical Conference and Exhibition. Denver, Colorado, U.S.A, pp. 5–8 October 2003. SPE-84590-MS.

AlQuaimi, B.I., Rossen, W.R., 2017a. Capillary desaturation curve for residual nonwetting phase in natural fractures. SPE J. https://doi.org/10.2118/189448-PA.

AlQuaimi, B.I., Rossen, W.R., 2017b. Characterizing foam flow in fractures for enhanced oil recovery. In: Paper Presented at the 19th European Symposium on Improved Oil Recovery, Stavanger, Norway.

AlQuaimi, B.I., Rossen, W.R., 2017c. New capillary number definition for displacement of residual nonwetting phase in natural fractures. Geophys. Res. Lett. https://doi.org/10.1002/2017GL073211.

Alvarez, J.M., Rivas, H.J., Rossen, W.R., 2001. Unified model for steady-state foam behavior at high and low foam qualities. SPE J. https://doi.org/10.2118/74141-PA.

Alverez, J., Rivas, H., Rossen, W., 1999. A unified model for steady-state foam behavior at high and low foam qualities. In: Paper Presented at the IOR 1999–10th European Symposium on Improved Oil Recovery.

Babadagli, T., 2001. Selection of proper EOR method for efficient matrix recovery in naturally fractured reservoirs. In: Paper Presented at the SPE Latin American and Caribbean Petroleum Engineering, Buenos Aires, Argentina.

Bernard, G.G., Holm, L.W., 1964. Effect of foam on permeability of porous media to gas. SPE J. 4 (3), 267–274. https://doi.org/10.2118/983-PA.

Bertotti, G., Immenhauser, A., Koppen, J.K.J., T.-v, 2005. Stratigraphic and regional distribution of fractures in Barremian–Aptian carbonate rocks of Eastern Oman: outcrop data and their extrapolation to Interior Oman hydrocarbon reservoirs. Int. J. Earth Sci. 94 (3), 447–461. https://doi.org/10.1007/s00531-005-0472-5.

Bourbiaux, B., Fourno, A., Nguyen, Q.-L., Norrant, F., Robin, M., Rosenberg, E., Argillier,

J.-F., 2016a. Experimental and numerical assessment of chemical enhanced oil recovery in oil-wet naturally fractured reservoirs. SPE J. 21 (3). https://doi.org/10.2118/169140-PA.
Bourbiaux, B., Rosenberg, E., Robin, M., Chabert, M., Chevallier, E., Gautier, S., 2016b. Computed-tomography-scan Monitoring of Foam-based Chemical-enhanced-oil-recovery Processes in Fractured Carbonate Cores. https://doi.org/10.2118/179811-PA.
Buchgraber, M., Castanier, L.M., Kovscek, A.R., 2012. Microvisual investigation of foam flow in ideal fractures: role of fracture aperture and surface roughness. In: Paper Presented at the SPE Annual Technical Conference and Exhibition.
Chen, C.Y., Horne, R.N., Fourar, M., 2004a. Experimental study of liquid-gas flow structure effects on relative permeabilities in a fracture. Water Resour. Res. 40 (8). https://doi.org/10.1029/2004WR003026. W08301.
Chen, C.Y., Li, K., Horne, R.N., 2004b. Experimental study of phase transformation effects on relative permeabilities in fractures. In: Paper Presented at the SPE Annual Technical Conference and Exhibition.
Cussler, E.L., 2009. Diffusion: Mass Transfer in Fluid Systems. Cambridge university press, Cambridge, UK.
Ettinger, R., Radke, C., 1992. Influence of texture on steady foam flow in berea sandstone. SPE Reservoir Eng. 7 (01), 83–90.
Farajzadeh, R., Muruganathan, R., Rossen, W., Krastev, R., 2011. Effect of gas type on foam film permeability and its implications for foam flow in porous media. Adv. Colloid Interface Sci. 168 (1), 71–78.
Ferno, M.A., Gauteplass, J., Pancharoen, M., Haugen, Å., Graue, A., Kovscek, A.R., Hirasaki, G., 2016. Experimental study of foam generation, sweep efficiency, and flow in a fracture network. SPE J. 21 (4), 1140–1150. https://doi.org/10.2118/170840-PA.
Fourar, M., Bories, S., Lenormand, R., 1992. Experimental study of two-phase flow in rough fractures. In: Proceedings, Seventeenth Workshop on Geothermal Reservoir Engineering. Stanford University, Stanford, California, pp. 215–218.
Gauteplass, J., Chaudhary, K., Kovscek, A.R., Fernø, M.A., 2015. Pore-level foam generation and flow for mobility control in fractured systems. Colloid. Surface. Physicochem. Eng. Aspect. 468, 184–192.
Hakami, E., Larsson, E., 1996. Aperture measurements and flow experiments on a single natural fracture. In: Paper Presented at the International Journal of Rock Mechanics and Mining Sciences & Geomechanics Abstracts.
Haugen, Å., Fernø, M.A., Graue, A., Bertin, H.J., 2012. Experimental study of foam flow in fractured oil-wet limestone for enhanced oil recovery. SPE Reservoir Eval. Eng. 15 (02), 218–228.
Haugen, Å., Mani, N., Svenningsen, S., Brattekås, B., Graue, A., Ersland, G., Fernø, M.A., 2014. Miscible and immiscible foam injection for mobility control and EOR in fractured oil-wet carbonate rocks. Transport Porous Media 104 (1), 109–131.
Holm, L.W., 1968. The mechanism of gas and liquid flow through porous media in the presence of foam. SPE J. 8 (4), 359–369. https://doi.org/10.2118/1848-PA.
Hughes, R.G., Blunt, M.J., 2001. Network modeling of multiphase flow in fractures. Adv. Water Resour. 24 (3–4), 409–421. https://doi.org/10.1016/S0309-1708(00)00064-6.
Huh, D.G., Handy, L.L., 1989. Comparison of steady and unsteady-state flow of gas and foaming solution in porous media. SPE Reservoir Eng. 4 (1), 77–84. https://doi.org/10.2118/15078-PA.
Khatib, Z., Hirasaki, G., Falls, A., 1988. Effects of capillary pressure on coalescence and phase mobilities in foams flowing through porous media. SPE Reservoir Eng. 3 (03), 919–926.
Kim, J., Dong, Y., Rossen, W.R., 2005. Steady-state flow behavior of CO2 foam. SPE J. 10 (04), 405–415.
Kovscek, A., Tretheway, D., Persoff, P., Radke, C., 1995. Foam flow through a transparent rough-walled rock fracture. J. Petrol. Sci. Eng. 13 (2), 75–86.
Lenormand, R., Zarcone, C., Sarr, A., 1983. Mechanisms of the displacement of one fluid by another in a network of capillary ducts. J. Fluid Mech. 135, 337–353.
Manrique, E.J., Muci, V.E., Gurfinkel, M.E., 2007. EOR field experiences in carbonate reservoirs in the United States. SPE Reservoir Eval. Eng. 10 (6). https://doi.org/10.2118/100063-PA.
Narr, W., Schechter, D.W., Thompson, L.B., 2006. Naturally Fractured Reservoir Characterization. Society of Petroleum Engineers, Richardson, TX.
Nonnekes, L.E., Cox, S.J., Rossen, W.R., 2015. Effect of gas diffusion on mobility of foam for enhanced oil recovery. Transport Porous Media 106 (3), 669–689.
Ozkaya, S.I., 2007. Detection of fracture corridors from openhole logs in horizontal wells. In: Paper Presented at the SPE Saudi Arabia Section Technical Symposium, Dhahran, Saudi Arabia, SPE-110942-MS.
Pieters, D., Graves, R., 1994. Fracture relative permeability: linear or non-linear function of saturation. In: Paper Presented at the International Petroleum Conference and Exhibition of Mexico.
Pruess, K., Tsang, Y.W., 1990. On two-phase relative permeability and capillary pressure of rough-walled rock fractures. Water Resour. Res. 26 (9), 1915–1926. https://doi.org/10.1029/WR026i009p01915.
Pyrak-Nolte, L.J., Cook, N.G., Nolte, D.D., 1988. Fluid percolation through single fractures. Geophys. Res. Lett. 15 (11), 1247–1250.
Qian, J., Chen, Z., Zhan, H., Guan, H., 2011. Experimental study of the effect of roughness and Reynolds number on fluid flow in rough-walled single fractures: a check of local cubic law. Hydrol. Process. 25 (4), 614–622.
Rabbani, A., Jamshidi, S., Salehi, S., 2014. An automated simple algorithm for realistic pore network extraction from micro-tomography Images. J. Petrol. Sci. Eng. 123, 164–171.
Ransohoff, T., Radke, C., 1988. Mechanisms of foam generation in glass-bead packs. SPE Reservoir Eng. 3 (02), 573–585.
Rossen, W.R., 1996. Foams in enhanced oil recovery. Surfactant Sci. Ser. 413–464.
Rossen, W.R., 2003. A critical review of Roof snap-off as a mechanism of steady-state foam generation in homogeneous porous media. Colloid. Surface. Physicochem. Eng. Aspect. 225 (1), 1–24.
Rossen, W., Kumar, A.T., 1992. Single-and two-phase flow in natural fractures. In: Paper Presented at the SPE Annual Technical Conference and Exhibition, Washington, D.C., USA.
Skoreyko, F.A., Villavicencio, A.P., Rodriguez Prada, H., Nguyen, Q.P., 2011. Development of a new foam EOR model from laboratory and field data of the naturally fractured Cantarell field. In: Paper Presented at the SPE Reservoir Characterisation and Simulation Conference and Exhibition.
Steinsbø, M., Brattekås, B., Ersland, G., Bø, K., Opdal, I., Tunli, R., et al., 2015. Foam as mobility control for integrated CO2-EOR in fractured carbonates. In: Paper Presented at the IOR 2015–18th European Symposium on Improved Oil Recovery, Dresden, Germany, pp. 14–16 April 2015.
Tsang, Y., 1984. The effect of tortuosity on fluid flow through a single fracture. Water Resour. Res. 20 (9), 1209–1215.
Witherspoon, P.A., Wang, J.S., Iwai, K., Gale, J.E., 1980. Validity of cubic law for fluid flow in a deformable rock fracture. Water Resour. Res. 16 (6), 1016–1024.
Yan, W., Miller, C.A., Hirasaki, G.J., 2006. Foam sweep in fractures for enhanced oil recovery. Colloid. Surface. Physicochem. Eng. Aspect. 282, 348–359.